Energy 323 (2025) 135615

Contents lists available at ScienceDirect

Energy

journal homepage: www.elsevier.com/locate/energy

Discretization modeling with pseudo real-time waves input of the hybrid wave-tidal energy converter based on non-linear motions rectification and coupling device

Peihao Chen [a], Dawei Wu [a,*], Yiqing Yang [b], Athanasios Tsolakis [a]

[a] Department of Mechanical Engineering, University of Birmingham, Birmingham, B15 2TT, United Kingdom
[b] School of Mechanical Engineering and Automation, Beihang University, Beijing, 100191, China

ARTICLE INFO

Handling Editor: Prof G Iglesias

Keywords:
Discretization modeling
Wave energy converter
Tidal energy
Hybrid energy
Mechanical motion rectifier
Simulation

ABSTRACT

The discretization modeling methodology is proposed for dynamic analysis of Hybrid Wave-Tidal Energy Converters (HWTEC). By integrating the Pseudo Real-Time Wave (PRTW) simulation method based on random wave theory, it effectively reflects the actual random ocean waves characteristics and addresses the nonlinear response, without relying on continuous inputs. The discretization modeling method precisely determines and calculates the nonlinear dynamic response during the overrunning phase, enabling direct numerical solutions for nonlinear input and output parameters in the time domain, and eliminating the need for complex manual judgments. Validation through re-simulation of previous work shows an acceptable error of approximately 5 % in input and 0.5 % in output, demonstrating reliability. The proposed hybrid wave-tidal energy converter, based on the Non-Linear Motions Rectification and Coupling Device (NLMRCD), converts reciprocating wave motion into one-way motion and couples it with tidal rotation to enhance power output. It leverages the complementary and asynchronous distribution of wave and tidal energies, resulting in more stable output. Simulations reveal the impact of key parameters on output power and efficiency, achieving an average output power of 206.2 W and an efficiency of 40.8 %. The overrunning phase increases output power by 54.0 %, significantly enhancing output stability.

Nomenclature

ω_{in1}	angular velocity of input shaft #1 in the NLMRCD, rad/s
ω_{in2}	angular velocity of input shaft #2 in the NLMRCD, rad/s
ω_{out}	angular velocity of the output shaft in the NLMRCD, rad/s
n	transmission ratio in the NLMRCD
h	water depth, m
λ	wavelength, m
H	wave height, m
$\bar{H}_{1/3}$	significant wave height, m
$\bar{T}_z$	average zero-crossing period, s
V_{dww}	wave speed in deep water, m/s
f_{dww}	wave frequency in deep water, Hz
g	gravity acceleration, m/s^2
v	velocity of buoy under wave driving, m/s
t	time, s
a	acceleration of buoy under wave driving, m/s^2
ω_1	input angular velocity of input shaft #1, rad/s
ω_2	input angular velocity of input shaft #2, rad/s
r_{owg}	base circle radius of the one-way gear, m
ω'_1	output angular velocity of input shaft #1, rad/s
α_1	angular acceleration of the wave driving parts, rad/s^2
α_3	angular acceleration of the driven parts, rad/s^2
M_{in1}	input torque of the input shaft #1, N·m
M_{d1}	friction torque of the wave driving parts, N·m
J_1	inertia of the wave driving parts, kg·m^2
M_{d3}	friction torque of the driven parts, N·m
J_3	inertia of the driven parts, kg·m^2
c_1	viscous damping coefficient of the wave driving parts, N·s
M_{in2}	input torque of the input shaft #2, N·m
M_{d2}	friction damping torque of the input shaft #2, N·m
c_2	viscous damping coefficient of the input shaft #2, N·s
c_3	electrical damping coefficient of the generator, N·s
U	voltage generated from the generator, V
k_e	back electromotive voltage coefficient, V·s/rad

(continued on next page)

* Corresponding author. Department of Mechanical Engineering, University of Birmingham, B15 2TT, United Kingdom.
E-mail address: d.wu.1@bham.ac.uk (D. Wu).

https://doi.org/10.1016/j.energy.2025.135615
Received 27 July 2024; Received in revised form 21 December 2024; Accepted 12 March 2025
Available online 20 March 2025

(*continued*)

k_t	torque coefficient of the generator, V·s
M_e	electrical damping torque of the generator, N·m
$J_{input\text{-}shaft\text{-}1}$	inertia of input shaft #1, kg·m^2
$J_{input\text{-}shaft\text{-}2}$	inertia of input shaft #2, kg·m^2
$J_{bevel\text{-}gear\text{-}rotation}$	inertia of the bevel gear in rotation, kg·m^2
$J_{bevel\text{-}gear\text{-}revolution}$	inertia of the bevel gear in revolution, kg·m^2
$J_{small\text{-}gear}$	inertia of the small gear engaged with the frame, kg·m^2
$J_{large\text{-}gear}$	inertia of the large gear on the frame, kg·m^2
J_{frame}	inertia of the frame, kg·m^2
$J_{output\text{-}shaft}$	inertia of the output shaft, kg·m^2
$J_{side\text{-}shaft\text{-}rotation}$	inertia of the side shaft in rotation, kg·m^2
$J_{side\text{-}shaft\text{-}revolution}$	inertia of the side shaft in revolution, kg·m^2
$J_{one\text{-}way\text{-}gear}$	inertia of the one-way gear, kg·m^2
$J_{roller\text{-}bearing\text{-}inner\text{-}ring}$	inertia of the roller bearing inner ring, kg·m^2
$J_{washer\text{-}rotation}$	inertia of the washer in rotation, kg·m^2
$J_{washer\text{-}revolution}$	inertia of the washer in revolution, kg·m^2
$J_{flange\text{-}bearing\text{-}inner\text{-}ring\text{-}rotation}$	inertia of the flange bearing inner ring in rotation, kg·m^2
$J_{flange\text{-}bearing\text{-}revolution}$	inertia of the flange bearing in revolution, kg·m^2

1. Introductions

Sustainable and renewable energy sources are essential in achieving global decarbonization and realizing a zero-carbon future. Wave energy and tidal energy are widely distributed in ocean, which attracts lots of research interest.

In order to harness the kinetic and potential energy in waves and tides, Wave Energy Converter (WEC) and Tidal Energy Converter (TEC) have been designed and studied for many years [1–3]. The WEC utilizing bevel gear mechanical motion rectifier (MMR) are proposed, tested and demonstrate good performance in both dry lab experiments and wave tank tests [4,5]. Similarly, WEC employing rack-pinion MMR [6] and two-leg MMR [7] are also successfully developed and perform effectively. However, the intermittent generation and instability of single-source energy systems have always been challenges. Recently, the combination of wave energy and tidal energy has been attracting attention, aiming to improve the discontinuity and instability of single wave or tidal energy and reduce the cost with more output power [8,9]. Chen and Wu reviewed the state of Hybrid Wave-Tidal Energy Converters (HWTEC), and pointed out that proper coupling of wave energy capturing module and tidal energy capturing module can improve the output power, efficiency and output stability [10]. The review explains the potential of HWTEC in optimizing energy harnessing but also reveals significant challenges in device design. The HWTEC can be divided into non-coupling devices and coupling devices. Non-coupled HWTECs, such as the hydro-kite-like energy converter [11], the HWTEC based on oscillating buoy and vertical-axis turbine [9] and the HWTEC based on overtopping module and oscillating water column module [12], are constructed by combining wave energy converter and tidal energy converter directly or by switching modes during operation. These studies primarily emphasize innovative designs and performance while often neglecting the potential negative interactions and incompatibilities between modules. For example, parameters optimized for one operational mode may not be suitable for another, and the tidal energy capture module could disrupt the hydrodynamic performance of the wave energy capture module, leading to a reduction in overall efficiency. Coupling devices can improve these issues to a certain extent by utilizing the coupling between different energy capture modules. A wave-current hybrid energy converter based on the bevel gear mechanical motion rectifier can only engage the higher input speed among wave input and tidal input at any given time, and disengage the lower one, to make full use of the complementarity between them and increase the output stability [13–15]. However, actively discarding the lower one of wave and tidal energy leads to reduce the overall energy utilization. The coupling effect contribute to improvement in output power in the HWTEC based on horizontal cylinder and swing plate [16] and muti-degree-of-freedom hybrid system [17]. In these cases, the operation of one of the energy capture modules extends the work bandwidth or stroke of another module, which harvests more energy than working separately. The hybrid WEC based on an Oscillating Water Column (OWC) and an Oscillating Buoy (OB) [18] is proposed, accounting for the hydrodynamic interactions between the modules. The study concludes that hybrid energy converters can enhance both energy conversion and wave attenuation. Hydrodynamic analysis in Ref. [19] further examines the effects of wave parameters and WEC design parameters on module interactions using a one-way coupling approach. It highlights an important aspect beyond device coupling: the mutual influence and coupling in hydrodynamics.

Despite these advancements, significant challenges remain in the modeling and simulation of HWTEC under real ocean conditions. In modeling and simulation, linear modeling methods widely used are based on dynamical general equations and ideal continuous input hypotheses, which are simple to establish especially for those non-coupling devices. The single-floating body system [20,21], the double-floating body [22] and the bond graph (BG) modeling method [9] are typical linear systems. While with the rising of coupling devices and requirements for accurate performance analysis, nonlinear modeling methods inevitably becomes an important research approach. In order to solve the speed response function during the overrunning phase of one-way bearings, piecewise functions are established to represent the meshing phase and overrunning phase [23–26]. Since the input velocity is set as sinusoidal, the continuity enables the numerical solution of acceleration and power. In more complex cases where there are more nonlinear factors, it is hard to get the numerical solution. The variable inertia in Refs. [26,27] decides that the velocity response must be represented as an implicit function. The use of the continuity equation as input is fundamental for determining boundary conditions, but the simplicity of idealized sinusoidal inputs and the absence of real wave inputs often obscure the critical need for discretized modeling. In fact, real ocean inputs are typically complex, random and uncertain. This reliance on continuity equation input limits current modeling approaches, rendering them inadequate for capturing the dynamics under real ocean conditions, thereby creating a gap between theoretical simulations and actual ocean environments. To address these challenges, both a nonlinear discretization modeling methodology and the simulation of real ocean waves are essential.

To compensate for the distortion of input data, it is necessary to explore alternative sources of real wave data and incorporate advanced simulation methods that can approximate real ocean conditions more effectively. The real-time wave data can be obtained from monitoring stations, such as the National Network of Regional Coastal Monitoring Programmes of England. However, the observation points only cover a small part of the ocean and are mainly concentrated in near offshore areas, where wave energy distribution differs from that in far open sea. Real-time wave simulation has been a hot topic in the field of computer graphics, which can partially make up for the missing data to a certain extent and promote the simulation research on wave energy conversion. In computer graphics, there are three common approaches to simulate the ocean surface wave, i.e., geometrical description models, spectral description models, and physically based models from Computational Fluid Dynamics [28,29]. Current wave simulation in the field of computer graphics focuses on the surface texture to make it look real [30–32]. JONSWAP spectrum is often used for the wave spectra growing in fetch-limited conditions, and mainly focuses on certain frequency bands [33]. Simulation of wind-driven ocean waves in the deep ocean is proposed by Ref. [29], which can be utilized to simulate the interaction between ocean waves and floating bodies based on physical models. For dynamic analysis of marine device, the interaction between waves and the hardware is the key factor. Therefore, advanced methodologies, such as particle system dynamics simulation and wave spectrum simulation, are not necessary and even too difficult to calculate. However, current wave energy conversion research still requires the sine wave assumption, which creates a significant gap between the ideal assumption and the more realistic wave simulation methods discussed above. Bridging this gap is an urgent priority. Therefore, it is valuable to draw on the understanding of wave shape characteristics and motion dynamics in computer graphics to simplify and extract methods that effectively reflect the dynamic characteristics of real waves and adapt them to simulate real-time waves behavior in wave energy conversion. This methodology of simulating real-time response of waves in the time domain will be proposed in this paper, which is named the simulation of Pseudo Real-Time Waves (PRTW).

In summary, in the current research on hybrid wave-tidal energy conversion, since the sinusoidal wave assumption has always been used, the conditions for modeling and analysis of the energy converter are far from the actual operating conditions. A common modeling approach involves utilizing sine wave inputs into the wave energy converter modeling based on the continuity equation, resulting in the need to find boundary conditions artificially in some complex nonlinear situations and making the solution difficult. Consequently, the introduction of discretized modeling methods can not only greatly reduce the difficulty of accurately solving dynamic modeling, but also extend the input conditions from the continuity equation to arbitrary waveform input, allowing real ocean wave data can be fed into the simulation. Therefore, focusing on the field of hybrid wave-tidal energy conversion, this paper proposes a discretized modeling method based on time domain and validates it with previous work. Meanwhile, a novel PRTW simulation is proposed as input to the discretized model. Finally, the Non-Linear Motions Rectification and Coupling Device (NLMRCD) is designed to improve output power and stability in dual inputs requirement scenario, like hybrid wave-tidal energy conversion, by rectifying wave reciprocating motion into one-way linear motion and coupling it with tidal rotation together to utilize their complementary. The performance prediction of the device is performed using above simulation methods. The rest of the paper is organized as follows. Section 2 introduces the hardware design on which the modeling is based, including the previously proposed wave energy converter (WEC) and the NLMRCD. The modeling methodology is introduced in Section 3 and is validated by remodeling the previous work in Section 4. The methodology proposed is utilized to predict and analyze the dynamic characteristics of the HWTEC based on NLMRCD in Section 5. And the paper is concluded in Section 6.

2. Design of WEC and HWTEC

The authors previously proposed the WEC based on a Coaxial Mechanical Motion Rectifier, which is used to validate the newly proposed modeling methods in this work. The HWTEC, based on Non-Linear Motions Rectification and Coupling Device, is detailed and serves as the primary focus of the current analysis.

2.1. WEC based on Coaxial Mechanical Motion Rectifier (CMMR)

A WEC based on the Coaxial Mechanical Motion Rectifier (CMMR) is designed, simulated and tested in dry lab and real sea [26]. The core parts of the WEC include the ball screw transmission module, CMMR, generator with variable inertia flywheel (VIF). The wave energy is captured by a buoy in the form of up and down motion and converted into reciprocating rotation by the ball screw transmission module. The CMMR then converts it into one-way rotation to drive the generator with VIF.

The CMMR based on the planetary gear train parts and four one-way bearings operates in two respective states when the input rotating direction changes (Fig. 1). When the input shaft rotates clockwise (Fig. 1 (b)), one-way bearings L1 and S2 are engaged while others are disengaged, fixing the input shaft with planet carrier, causing the output shaft to rotate clockwise. When the input shaft rotates counterclockwise (Fig. 1 (c)), one-way bearing L2 and S1 are engaged while others are

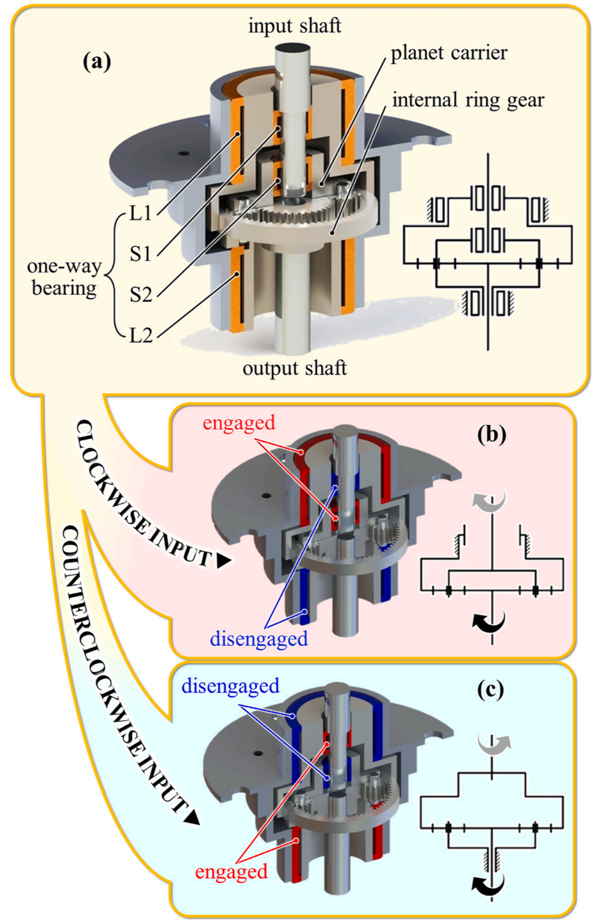

Fig. 1. Working principle of the CMMR. (a) Overall indication. (b) Clockwise input state. (c) Counterclockwise input state.

disengaged, fixing the input shaft with internal ring gear, causing the output shaft to rotate clockwise. Since the engaging directions of S1 and S2 on input shaft are the same, an overrunning phase occurs when the velocity and acceleration of the input shaft are both lower than those of the planet carrier or the internal ring gear, which is the nonlinear response. The CMMR with overrunning phase reduces energy loss during frequent mechanical motion direction switches, with the effect becoming more pronounced with greater change in acceleration.

Building on this foundation, the energy storage and buffering functions of the VIF further also contribute to smoothing the output speed. While the nonlinear variation in inertia of the VIF during acceleration deceleration inevitably complicates the nonlinear modeling.

2.2. Hybrid wave-tidal energy converter (HWTEC)

The HWTEC proposed in this work is designed to capture the wave energy and tidal energy at the same time and coupling them together to output a summed speed and power. Wave energy is mainly generated from the vertical heave motion of sea surface water, while tidal energy arises from the periodic horizontal flow of seawater at depth [34], hence a rack-and-pinion mechanism and a turbine with a horizontal shaft are chosen to transmit mechanical energy. The buoy module captures the reciprocating linear motions from waves, while the turbine module captures the one-way rotation from tide, both transferring energies to the Non-Linear Motions Rectification and Coupling Device (NLMRCD). The NLMRCD converts the reciprocating motions into one-way rotation and couples the two rotations into a summed output to drive the generator.

The NLMRCD is designed based on a bevel gearbox, rack-and-pinion sets and one-way bearings to rectify reciprocating mechanical motions into one-way and couple the two speeds together (Fig. 2). Depending on the input speeds, it can be equipped with either single or double mechanical motion rectifier. Single mechanical motion rectifier can handle scenarios where one of the inputs is reciprocating motion and another is one-way motion, whereas double mechanical motion rectifiers is suited for scenarios where both inputs are reciprocating motions. In this case, the single is selected as the core part of the HWTEC proposed in this work.

The system comprises two input shafts. Input shaft #1, along with one-way bearings installed in the same engaging direction on it, constitutes the mechanical motion rectifier. Racks connected to the buoy module engage with the pinions fixed with the one-way bearings. When the buoy module moves down (Fig. 2 (a)) and up (Fig. 2 (b)), input shaft #1 always rotates clockwise and drives the frame of the bevel gearbox in counterclockwise. Additionally, the input shaft can continue rotating due to inertia when the driving acceleration from the one-way gears is less than the acceleration from damping, known as the overrunning phase. The overrunning phase improves the smoothness of speed and minimizes impact during frequent switches in motion direction. Input shaft #2 is connects to the turbine module, transferring the one-way rotation to drive the bevel gear clockwise in the bevel gearbox (Fig. 2 (c)). The relative motion between the frame and the bevel gear makes the speed summed at the output shaft. If the transmission ratio n between input shaft #1 and the gear box frame is n:1, the speeds ratio of the two input shafts during the linear phase will be $(2/n)$:1, which is written as,

$$\omega_{\text{out}} = \frac{2}{n}|\omega_{\text{in1}}| + \omega_{\text{in2}} \tag{1}$$

where ω_{in1}, ω_{in2} and ω_{out} are the angular velocity of input shaft #1, input shaft #2 and output shaft respectively. In this work, the transmission ratio n is set to 2:1. Finally, the system achieves rectification and coupling of the reciprocating motion from waves and the one-way rotation from tides. The benefit is that the two types of blue energy can complement each other to reduce the discontinuity and fluctuation, resulting in a larger and more stable power output compared to working separately.

The HWTEC is designed to capture tidal current energy in deep waters and wave energy on the ocean surface, necessitating a vertically extensive structure. It introduces unique challenges compared to other hybrid energy converters, such as hybrid wind-wave and wind-solar system. Additionally, the HWTEC requires deployment in regions rich in both tidal and wave energy, such as areas south and northeast of Great Britain, limiting suitable locations compared to single energy converters. While this study focuses on validating the HWTEC concept, further research is needed to refine its waterproofing and seawater corrosion resistance designs.

3. Modeling methodology

In the simulation of PRTW, a novel method is proposed based on Random Wave Theory and the trochoid equation to eliminate the distortion caused by the sinusoidal wave assumption and enhance the realism of wave simulation. The discretization modeling derived from the device design mentioned above is then defined, including the discretization logic, parameterization and the automatic determination of boundary conditions in the simulation.

3.1. Pseudo real-time waves (PRTW)

Current real-time wave data is mainly concentrated in near-shore ports and waterways. In these areas, shallower sea causes waves to have larger heights and less kinetic energy, which is low-quality and not suitable for large scale capture. The real-time wave data of open sea is rarely reported. Therefore, the simulation of PRTW in open (deep) sea is useful to assess and predict the behavior of WEC under conditions closer to reality.

In existing dynamic analysis of WEC, the shape of ocean waves is usually described as a “sine long-crested wave”, but the experimental observation indicates that “trochoid” with longitudinal component is more accurate in presenting wave shape in real ocean conditions with

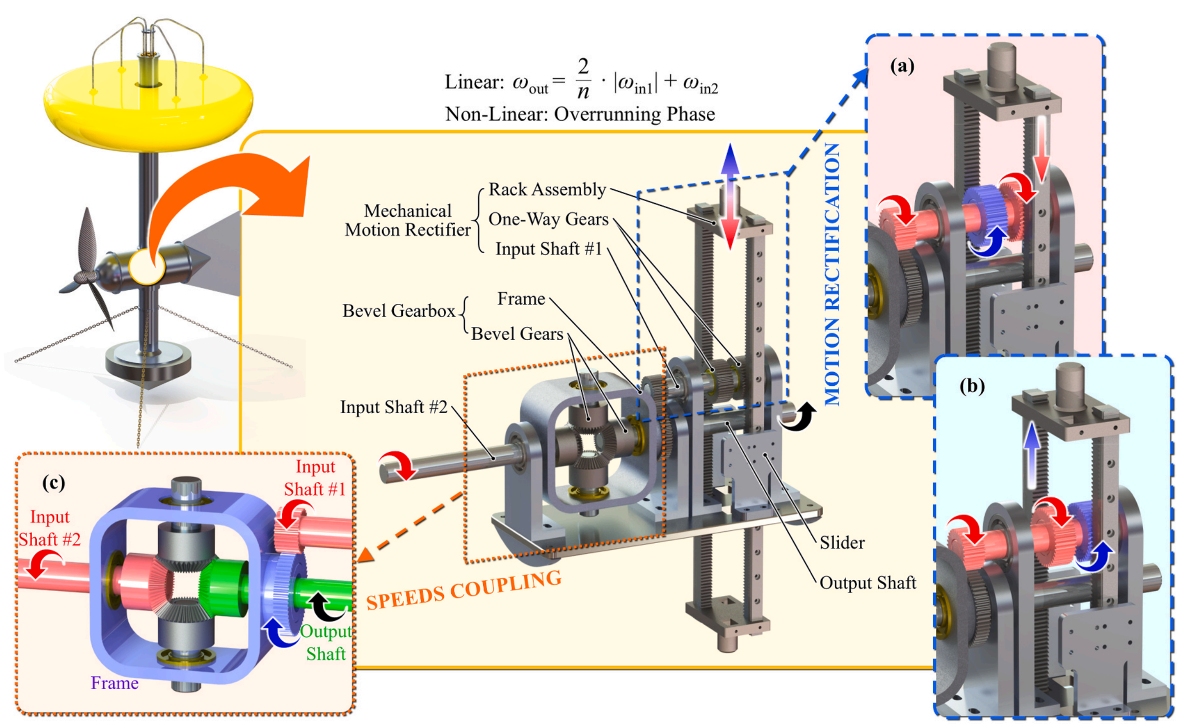

Fig. 2. Working principle of Non-Linear Motions Rectification and Coupling Device. (a) Mechanical Motion Rectifier when buoy module moves down. (b) Mechanical Motion Rectifier when buoy module moves up. (c) Speeds coupling in bevel gearbox.

wind [31,35]. The introduction of wave spectrum makes it possible to decompose a random wave into many sine waves by harmonic analysis or Fourier Transform (FT), which is effective in analyzing the overall characteristics of waves. Commonly used models of the spectrum have different emphasis [31,35]. Phillips' spectrum focuses on the shape of high frequency. Pierson-Moskowitz spectrum, considering wind speed, can describe idealized ocean waves with unlimited sampling duration. JONSWAP spectrum is often used for the wave spectra growing in fetch-limited condition. Texel-Marsen-Arsloe (TMA) spectrum considers the depth and is suitable for shallow ocean area. However, it is unrealistic and excessive to use FT for analyzing the dynamic response of the device to ocean waves in the time domain. Discretization of waves is usually used in the simulation of waves [36], hence it is reasonable to simulate the PRTW by discretization, which is relatively simpler than FT or spectrum and can ensure that it can be used as input to import the discretization modeling of the HWTEC directly.

Key parameters and terms are introduced here. In Gerstner wave model, the water particles move in vertical circles, which become smaller with increasing depth. When the depth h and wavelength λ meet $h>\lambda/4$, it can be regarded as deep water and under the depth of $\lambda/2$, the motion of water particles can be neglected [31]. As waves approach the coast, wavelength and speed decrease and only frequency remains constant. According to a theory of Stokes, waves break when the ratio of wave height H and wavelength λ is $H/\lambda > 1/7$. In reality, it usually occurs when $H/\lambda > 1/10$. And in this situation, the profile of the wave is more like a trochoid. And theoretically, the angle between the forward and backward slopes of waves at the crest is 120° when $H/\lambda = 1/7$. Therefore, for unbroken waves, the angle is larger than 120°. It is common to define ocean conditions by the significant wave height $\bar{H}_{1/3}$ (the average height of the 1/3 highest waves in a record, and close to the wave height observed visually) and the average zero-crossing period $\bar{T}_z$ [35]. In the Random Wave Theory, Rayleigh Distribution has been confirmed as a suitable representation for the distribution of wave height [35], and Gaussian noise (Gaussian distribution) is a classical method to generate random wave height in ocean simulation [28–31].

For deep water waves, the wave speed V_{dww} and the frequency f_{dww} can be estimated from following equations,

$$V_{\mathrm{dww}} = \sqrt{\frac{g\lambda}{2\pi}} \tag{2}$$

$$f_{\mathrm{dww}} = \frac{V_{\mathrm{dww}}}{\lambda} = \frac{g}{2\pi V_{\mathrm{dww}}} \tag{3}$$

where g is the gravity acceleration. The speed is determined by the wind and the rotation of the Earth, usually 1–200 m/s. The frequency is approximately 0.01–1 Hz. According to the wave data from National Data Buoy Center (Station 62050-E1, 50.0N 4.4W) on May 17, 2024, the significant wave height is mainly 1.0–1.6 m, and the dominant wave period is 2~6 s on that day. The pseudo real-time wave simulated based on these observation parameters is shown in Fig. 3, which depicts the instantaneous cross-sectional curve of the wave in space. The time step size is 0.001 s, which should be the same as the time step size in subsequent discretization modeling. 200 random numbers are generated to simulate 100 wave crests, because the slopes of the wave front and wave rear are different. By dividing this curve by the wave speed, the curve of the wave height at a fixed point changing with time can be obtained. The wave height conforms to a Normal Distribution with the mean of 1.3 and standard deviation of 0.3. The significant wave height conforms to a Rayleigh Distribution with the scale parameter of 1.6. The ratio of wave height and wavelength conforms to an Exponential Distribution with the minimum value of 10 and rate parameter of 1.

3.2. Discretization modeling

In previous work, reliance on the continuity equation primarily involved differentiating velocity function to obtain acceleration function, necessitating the calculation of global velocity and acceleration functions at every step. With the introduction of the overrunning phase and variable damping, acceleration is influenced not only by the input force but also by the current movement state. Consequently, the acceleration function cannot be solved analytically, requiring manual assessment of the nonlinear response.

It is known that in simulation software, the calculation of the continuity equation is also performed at each data point after dividing the equation into increments with a very small step size. As long as the step size is small enough and there are enough data points, it can be regarded as continuous. Hence, in the discretization modeling, the velocity function V is discretized to large number of data points with time increment Δt, every two adjacent data points v_n and $v_{(n\text{-}1)}$ are regarded as a small function. And the slope is the acceleration a_n, which is used to calculate the next velocity point $v_{(n+1)}$. The process can be written as

$$a_n = \frac{v_n - v_{(n-1)}}{\Delta t} \tag{4}$$

$$v_{n+1} = v_n + a_n \Delta t \tag{5}$$

A delay of duration Δt is introduced due to the misaligned integral, causing an error between the real dynamic response and the theorical value. Considering ocean waves have low frequency (usually 0.2 Hz–2.0 Hz), the magnitude of the error only depends on the time step size, which can be controlled under 1 %. In other words, the previous modeling method required the operation of the equation throughout the process, but in this work, it is simplified to the operation of data points. By this method, the solution of the acceleration and force in time domain can be obtained, the boundary conditions of nonlinear response can be judged automatically, and the input velocity can be extended to random wave. It can greatly simplify the computation in the WEC or HWTEC modeling and simulation, and obtain the nonlinear dynamic response of the device in the time domain directly. Combined with the input of pseudo real-time wave simulation, the dynamic characteristics of WEC or HWTEC close to real working conditions can be achieved.

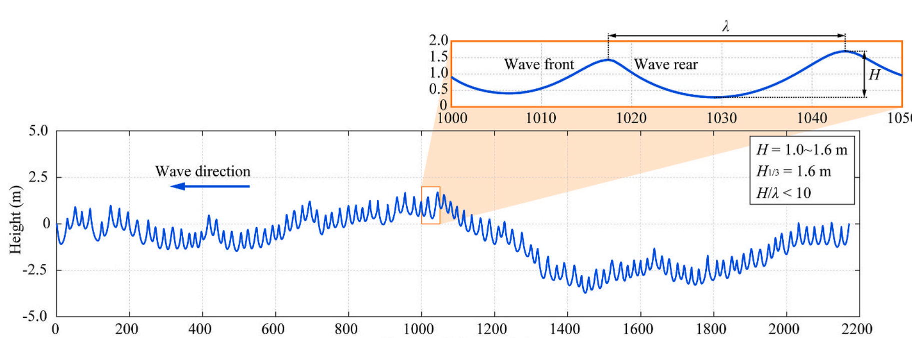

Fig. 3. Pseudo real-time wave simulated based on the observation data from Station 62050-E1.

Specifically, the modeling of the HWTEC proposed in this work is introduced following. The input velocity $v(t)$ of the buoy module and the angular velocity $\omega_1(t)$ of the input shaft #1 satisfies

$$\omega_1(t) = \left|\frac{v(t)}{r_{\mathrm{owg}}}\right| \tag{6}$$

where r_{owg} is the base circle radius of the one-way gear. The input angular velocity of the turbine and shaft #2 is $\omega_2(t)$. Due to the introduction of one-way bearings, the input shaft #1 can rotate faster than the one-way gears (i.e., overrunning phase). Here the output angular velocity $\omega'_1(t)$ of the input shaft #1 is introduced. In meshing phase, the transmission is linear. In overrunning phase, the output angular velocity $\omega'_1(t)$ of the input shaft #1 is larger than the input angular velocity $\omega_1(t)$ (Eq. (7)).

$$\begin{cases} \omega_1(t) = \omega'_1(t) \text{ (meshing phase)} \\ \omega_1(t) < \omega'_1(t) \text{ (overrunning phase)} \end{cases} \tag{7}$$

The output angular velocity $\omega_{\mathrm{out}}(t)$ of the NLMRCD is

$$\omega_{\mathrm{out}} = \frac{2}{i}\omega'_1 + \omega_2 \tag{8}$$

where the transmission ration i is set as 2 in this work. In order to make the non-linear relationship between the tidal driving parts, the wave driving parts and the driven parts clear, the device is considered in three modules (Fig. 4).

Input shaft #1 rotates reciprocating. In meshing phase, the angular acceleration α_1 of the wave driving parts is equal to α_3 of the driven parts. And the friction torque M_{d1} and the inertia J_1 of the wave driving parts and the friction torque M_{d3} and the inertia J_3 of the driven parts are all counted. Therefore, the torque balance is

$$M_{\mathrm{in1}} = (J_1\alpha_1 + J_3\alpha_3) + (c_1\omega_1 + c_3\omega_{\mathrm{out}}) + (M_{\mathrm{d1}} + M_{\mathrm{d3}}) \tag{9}$$

where M_{in1} is the input torque of the input shaft #1. While in overrunning phase, the angular acceleration α_1 of the wave driving part is smaller than α_3 of the driven part. The torque balance of the wave driving part and of the driven part are written separately as

$$\begin{cases} M_{\mathrm{in1}} = J_1\alpha_1 + c_1\omega_1 + M_{\mathrm{d1}} \\ 0 = J_3\alpha_3 + c_3\omega_{\mathrm{out}} + M_{\mathrm{d3}} \end{cases} \tag{10}$$

where the viscous damping coefficient c_1 of the wave driving parts can be neglected. Input shaft #2 is connected to the turbine (tidal energy), which rotates at a constant velocity and the torque balance is

$$M_{\mathrm{in2}} = (c_2 + c_3)\omega_{\mathrm{out}} + M_{\mathrm{d2}} \tag{11}$$

where M_{in2}, M_{d2} are the input torque and the friction damping torque of the input shaft #2, c_3 is the electrical damping coefficient of the generator, and c_2 is the viscous damping coefficient of the input shaft #2, which is 0.2 N s/m and can be neglected in this work since the viscous damping is much smaller than the electrical damping. In above functions, the output velocity ω_{out} is the common parameter, hence the torques of the three shafts are affected by each other, which is the coupling effect in the HWTEC. After obtaining the output velocity and input torque, then the voltage generated from the generator is

$$U = k_{\mathrm{e}}\omega_{\mathrm{out}} \tag{12}$$

where k_{e} is the back electromotive voltage coefficient, which is approximately 48.8 V s/rad. And the electrical damping torque M_{e} of the generator is proportional to the rotation speed of the generator, written as

$$M_{\mathrm{e}} = c_3\omega_{\mathrm{out}} = \frac{k_{\mathrm{t}}k_{\mathrm{e}}\omega_{\mathrm{out}}}{R} \tag{13}$$

where k_{t} is the torque coefficient of the generator. As the damping force proportional to speed, the viscous damping force is much smaller than the electrical damping torque of the generator and can be ignored in this work. Hence, the electrical damping torque will be the decisive factor affecting the start and end of the overrunning phase.

Therefore, once the device and the input velocities are determined, the corresponding rotation velocity of the generator will affect the damping force. The damping force, in turn, affects the start and end of the overrunning phase, which consequently affects the rotation velocity of the generator. To resolve this loop, determining when the overrunning phase occurs is crucial. It is evident that the overrunning phase must coincide with the speed decrease of the driving part. The mass relationships between the parts involved in the overrunning phase are depicted in Fig. 5.

Before the overrunning phase,

$$\begin{cases} \dfrac{M_{\mathrm{in1}} - M_{\mathrm{d1}} - M_{\mathrm{mid}}}{J_1} = \dfrac{M_{\mathrm{mid}} - M_{\mathrm{d3}}}{J_3} = \dfrac{M_{\mathrm{in1}} - M_{\mathrm{d1}} - M_{\mathrm{d3}}}{J_1 + J_3} \\ \omega_1 = \omega'_1 \end{cases} \tag{14}$$

At the starting of the overrunning phase,

$$\begin{cases} M_{\mathrm{mid}} = 0 \\ \dfrac{M_{\mathrm{in1}} - M_{\mathrm{d1}}}{J_1} = \dfrac{-M_{\mathrm{d3}}}{J_3} \\ M_{\mathrm{in1}} \le \dfrac{-M_{\mathrm{d3}}J_1}{J_3} + M_{\mathrm{d1}} \\ \omega_1 = \omega'_1 \end{cases} \tag{15}$$

During the overrunning phase,

$$\begin{cases} M_{\mathrm{mid}} = 0 \\ \dfrac{M_{\mathrm{in1}} - M_{\mathrm{d1}}}{J_1} <=> \dfrac{-M_{\mathrm{d3}}}{J_3} \\ \omega_1 < \omega'_1 \end{cases} \tag{16}$$

At the ending of the overrunning phase,

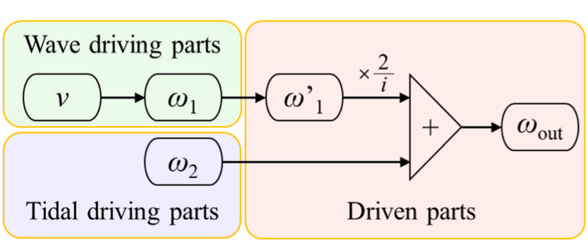

Fig. 4. Velocity relationship diagram.

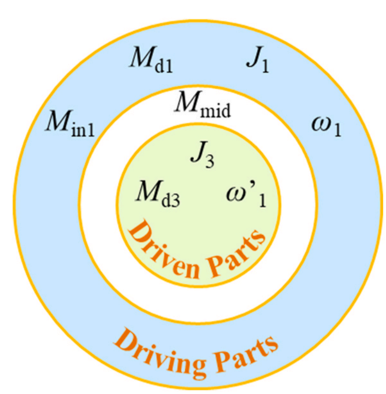

Fig. 5. Mass relationship between the parts involved in overrunning phase.

$$\frac{M_{\text{in1}} - M_{\text{d1}} - M_{\text{mid}}}{J_1} = \frac{M_{\text{mid}} - M_{\text{d3}}}{J_3} = \frac{M_{\text{in1}} - M_{\text{d1}} - M_{\text{d3}}}{J_1 + J_3} \tag{17}$$

And the judgment condition is as follows,

$$\begin{cases} \dfrac{M_{\text{in1}} - M_{\text{d1}}}{J_1} > \dfrac{-M_{\text{d3}}}{J_3} \\ \omega_1 = \omega_1' \end{cases} \tag{18}$$

According to above equations, the force equation of input shaft in every situation can be obtained. Values of the moment of inertia of the HWTEC are listed in Table 1.

4. Validation based on WEC

In the previous study on the WEC based on CMMR, the continuity equation of ideal sinusoidal velocity input was adopted and validated through lab tests and ocean experiments. In order to validate the discretization modeling methodology proposed in this work, it is applied to reanalyze the previous study.

The difference between the CMMR in Fig. 1 and the NLMRCD in Fig. 2 lies in the speeds coupling parts and the inertia changes in different working modes. The CMMR lacks speeds coupling, hence the second input velocity in the discretization modeling method is set to 0. The masses of rotation parts for clockwise and counterclockwise input are 79.8 g and 82.3 g respectively, which can be regarded approximately equal. The variable inertia related to velocity is calculated in Ref. [26] and can be directly substituted as a component of the inertia damping c_2 in Eq. (11). The discretization modeling theoretically accommodates these changes with minimal adjustments to the modeling programs. Other parameters of the WEC based on CMMR remain unchanged.

The sinusoidal velocity input is discretized with the time step size of 0.001 s. Since the simulation and experiment results of input force in Ref. [26] are expressed only with displacement, the results from discretization modeling method are transferred to the relationship of force-displacement for direct comparison (Fig. 6). The change trend of the input force from the discretization modeling aligns with that of previous modeling, but some minor differences are notable. In the previous modeling, the speed functions during the meshing phase and overrunning phase were defined as piecewise functions requiring manual determination of boundary conditions. Hence, fitting was necessary to account for the abrupt force change at the start of the overrunning phase, leading to some distortion (Fig. 6 (b)). In contrast, the discretization modeling simplifies this process, allowing automatic determination of the transition from the meshing to the overrunning phase by the simulation program, thereby avoiding fitting errors. The force during overrunning phase noticeably increases in the discretization modeling. This increase is primarily due to enhanced damping considered in this work, which was previously neglected due to scale limitations. The simulation key performance indices (KPI) listed and compared in Table 2 indicates that the error rate of the work done per cycle is under 6 % and the rate of the maximum force is under 5 %, which is acceptable. While the signal noise in the experiments introduce errors to the results, the discretization modeling simulated results shows good agreement with the previous experimental input force in terms of numerical value, change trends and the duration of overrunning phases. Considering that the previous modeling is found to have an error of about 5 % lower than the dry-lab experiment results in Ref. [26], the error of the discretization modeling here can be regarded as closer to real dry-lab experiment conditions. The simulation results align well with previous simulation and experiment findings based on continuous modeling method, demonstrating the reliability of the discretization modeling method, despite changing the simulation logic for the automatic judgement of nonlinear boundary conditions.

Correspondingly, the output voltages are simulated and compared as well (Fig. 7), with the frequency of 0.50 Hz and the amplitude of 0.25 m. The ratio of the minimum and maximum voltage, used to assess the stability of the output voltage [27] is presented in Table 3. The beginning and end of overrunning phase show close alignment between the previous modeling and discretization modeling, with the error ratio no more than 0.5 % (Fig. 7). The error in meshing phase decrease as the slope of voltage decreases, likely due to the step size delay in discretization modeling (Fig. 7 (a)). Errors are smaller in segments with smaller slopes compared to those with larger slopes. Additionally, the absolute voltage value the increases as the decrease of the slope, resulting in a lower error rate. While in overrunning phase, the non-linear response can be simulated directly in the discretization modeling. Compared to the complex manual segmentation judgments in previous modeling, an error rate within 0.5 % is acceptable and negligible.

In summary, errors in discretization modeling mainly arises from time step delays caused by misaligned integrals. Shortening the time increment Δt proves effective in controlling errors within an acceptable range. Given its simplicity and universality for various input, the discretization modeling emerges as a superior solution for the simulation of WECs or HWTECs. Moreover, its high compatibility with arbitrary inputs surpasses that of previous modeling. Therefore, through the re-simulation of the WEC based on CMMR, the discretization modeling is validated as correct and easier to implement. However, when selecting the time increment Δt, it is necessary to strike a balance between computational efficiency and error range. It is hard to select the proper Δt directly where continuous simulation cannot be performed, and then reducing t as much as possible will take a long time and have high requirements on computing hardware.

5. Simulation result discussion of HWTEC

Large wave height or frequency results in a significant input force on the buoy module, which requires a large buoy to carry it. However, the increased mass of a larger buoy hinders efficient wave energy capture. Hence, a transmission mechanism is necessary to appropriately reduce speed and increase torque. Here the transmission ratio of 4:1 is adopted.

5.1. With sine wave input

Ocean waves can be regarded as the superposition of sine waves, and previous studies have confirmed that reproducible sinusoidal inputs are effective in elucidating the relationship between input factors and output parameters. In this section, ideal sine wave input and constant tidal velocity input are employed. The amplitude A and frequency f of waves, along with the input tidal velocity R_2 determine the input power and output voltage directly, hence are simulated at different values to explore the respective influences, with results summarized in Fig. 8. Please see Appendix A for detailed results.

As the amplitude A of waves increases from 1.0 m to 1.6 m (Figs. 8 (a–1)), the average input power from waves increases from 193.9 W to 415.9 W, the input power from tides increases from 67.2 W to 128.2 W, and the output power increases from 106.6 W to 206.2 W when the total load resistance is 1.0 kΩ. A slight decrease in efficiency from 40.8 % to 37.9 % occurs. The maximum output voltage increases from 375.6 V to 525.6 V (Figs. 8 (b–1)), while the ratio of min-max voltage barely

Table 1
Moment of inertia of parts in HWTEC.

Parameters	Value (kg·m^2)	Parameters	Value (kg·m^2)
$J_{\text{input-shaft-1}}$	9.6×10^{-5}	$J_{\text{side-shaft-rotation}}$	5.4×10^{-6}
$J_{\text{input-shaft-2}}$	3.1×10^{-5}	$J_{\text{side-shaft-revolution}}$	2.9×10^{-4}
$J_{\text{bevel-gear-rotation}}$	6.1×10^{-5}	$J_{\text{one-way-gear}}$	2.8×10^{-5}
$J_{\text{bevel-gear-revolution}}$	5.4×10^{-4}	$J_{\text{roller-bearing-inner-ring}}$	2.7×10^{-6}
$J_{\text{small-gear}}$	4.3×10^{-6}	$J_{\text{washer-rotation}}$	2.5×10^{-6}
$J_{\text{large-gear}}$	5.5×10^{-5}	$J_{\text{washer-revolution}}$	4.0×10^{-5}
J_{frame}	9.4×10^{-4}	$J_{\text{flange-bearing-inner-ring-rotation}}$	2.2×10^{-6}
$J_{\text{output-shaft}}$	1.3×10^{-5}	$J_{\text{flange-bearing-revolution}}$	1.2×10^{-4}

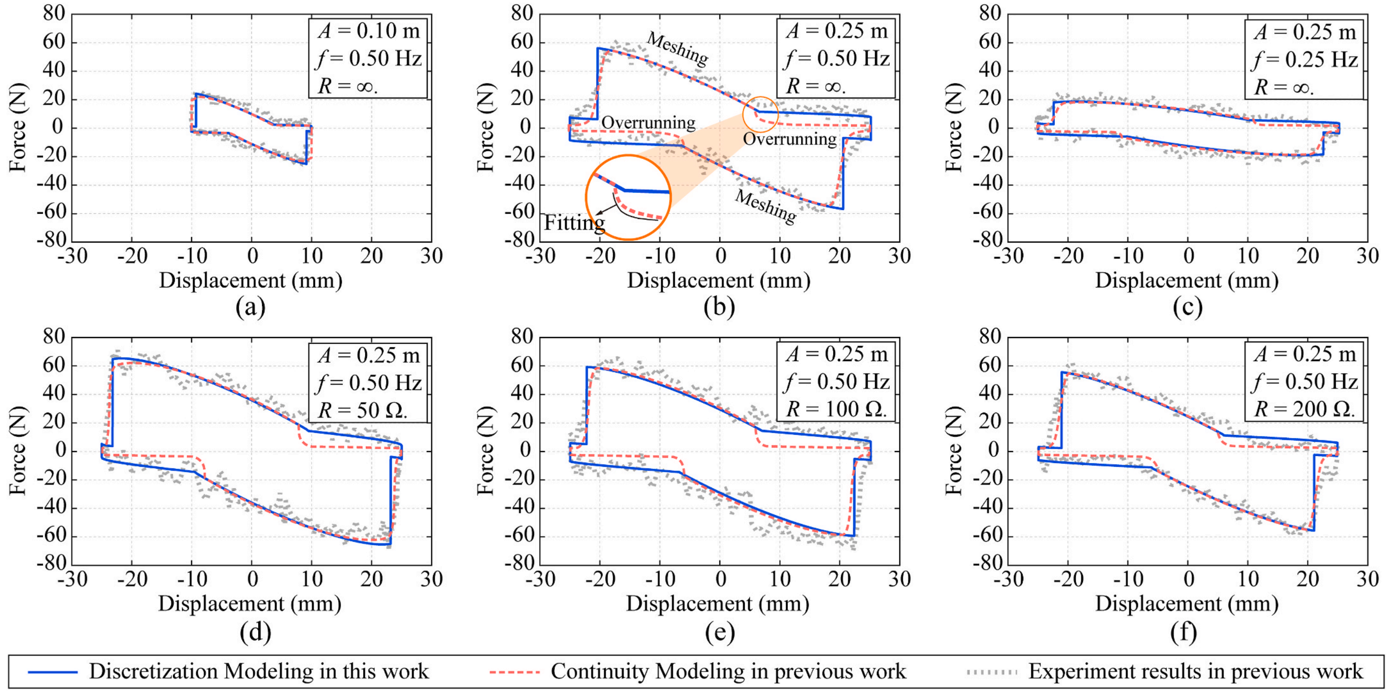

Fig. 6. Input force with different amplitude A, frequency f and external resistor R.

Table 2
Work, max force and error rate comparison between previous continuous modeling and discretization modeling.

Fig. No.	Work per Cycle (J)			Max Force (N)		
	Previous Modeling	Discretization Modeling	Error Rate	Previous Modeling	Discretization Modeling	Error Rate
(a)	4.43	4.26	−3.84 %	22.74	23.87	4.97 %
(b)	22.87	24.21	5.86 %	54.66	56.23	2.87 %
(c)	10.54	11.02	4.55 %	18.50	18.78	1.51 %
(d)	31.46	33.07	5.12 %	62.45	65.20	4.40 %
(e)	25.76	27.16	5.43 %	58.90	60.49	2.70 %
(f)	22.37	23.42	4.69 %	55.08	55.46	0.69 %

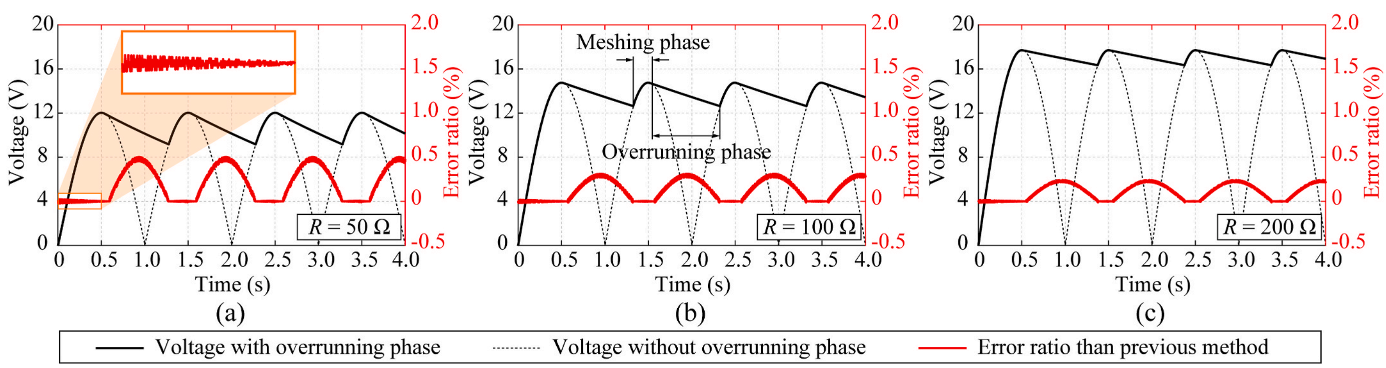

Fig. 7. Closed-circuit voltage with different external resistor R.

Table 3
Voltage and duration of overrunning phase in Fig. 7.

Fig. No.	Max Voltage (V)	Min Voltage (V)	Ratio of Min and Max Voltage	Duration of Overrunning Phase (s)
(a)	12.09	9.18	75.93 %	0.68
(b)	14.86	12.67	85.26 %	0.75
(c)	17.81	16.36	91.86 %	0.84

changes. In stable operation stage, the ratio of the overrunning phase in a cycle increases slightly from 60.6 % to 63.5 % (Figs. 8 (c–1)). The increase of amplitude of waves changes the speed proportionately with barely affecting the relationship between the input force/torque and the damping, making approximately proportionately increase of the voltage without obvious improvement in the stability of output voltage.

The increase of frequency f of waves makes the overall efficiency decrease obviously but cause ratio of min-max voltage and ratio of the overrunning phase increase sharply (Figs. 8 (a–2), (b-2) and (c-2)). Since the change of frequency does not affect the maximum output velocity,

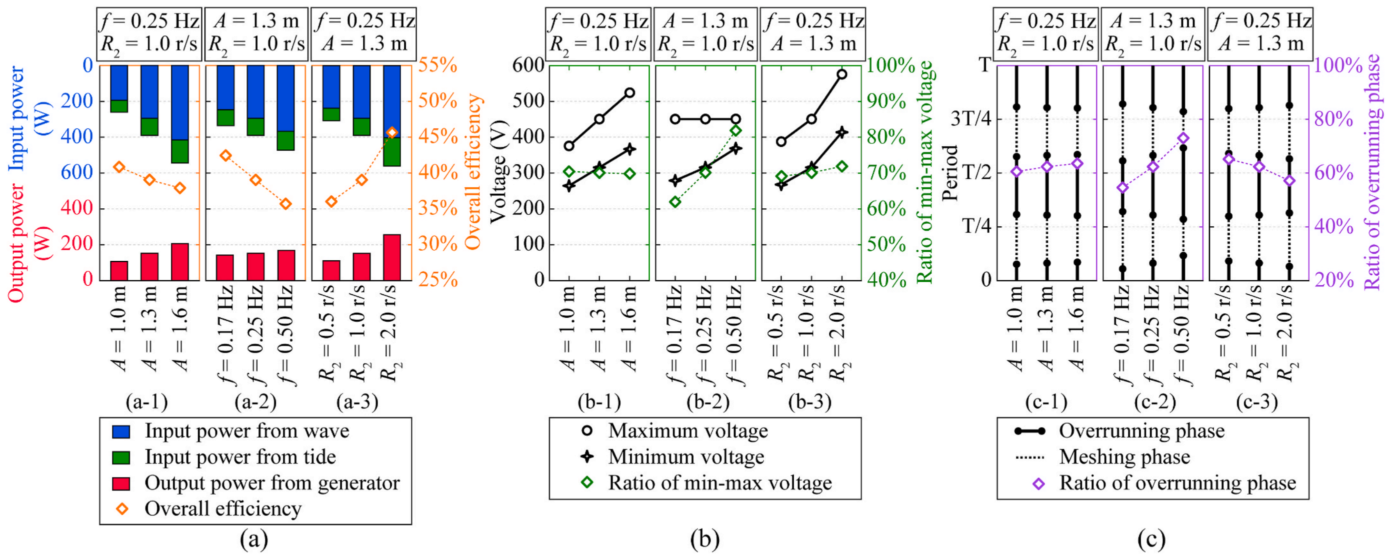

Fig. 8. Global view of simulation results. (a) Input power, output power and overall efficiency. (b) Maximum and minimum voltage and the ratio of min-max voltage. (c) Duration of overrunning phase and the ratio in a period.

the maximum voltage remains constant. High frequency extends the overrunning phase, so the minimum voltage increases much. However, higher frequency means higher speed, larger damping and more direction switches, which makes the overrunning phase play a greater role in improving the stability of output voltage.

While the increase of input tidal velocity R_2 greatly benefits to the overall efficiency and output voltage, and results in a minor increase in the ratio of min-max voltage, even though the ratio of overrunning phase decreases (Figs. 8 (a–3), (b-3) and (c-3)). The increase of tide velocity increases the damping slightly but decreases the proportion of waves in the inputs, causing shorter overrunning phase. And the tidal energy module which contains fewer transmission links has higher efficiency than the wave module, so it is a natural that a larger proportion of tidal energy in the inputs improves overall efficiency.

In summary, increasing wave amplitude primarily enhances output power and voltage, while increasing wave frequency mainly contributes to the stability of output voltage with minor improvements in power. However, both factors reduce overall efficiency. On the other hand, integrating tidal energy significantly improves both output power and efficiency, even though it has a limited impact on output voltage stability. It demonstrates that hybrid wave-tidal energy conversion can not only fully utilize these resources to increase output power, but also mitigate the asynchrony between power and efficiency.

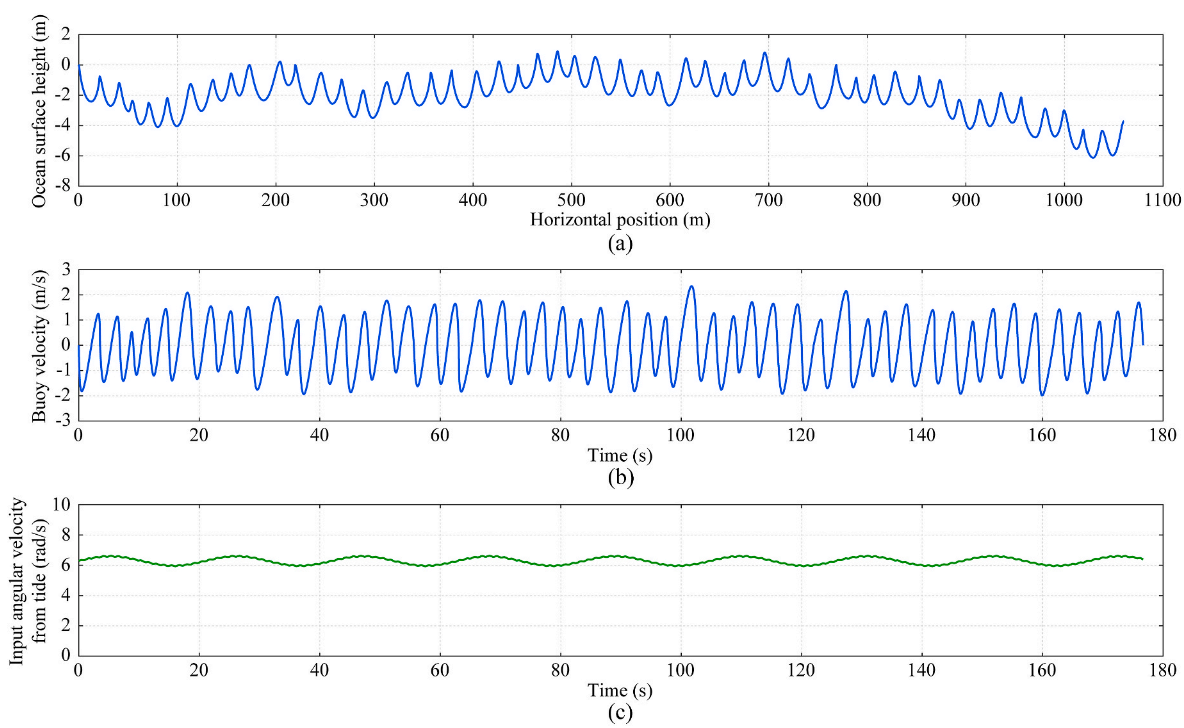

Fig. 9. (a) Shapes of PRTW. (b) Buoy velocity, i.e., the input speed from wave. (c) Input angular velocity from tide.

5.2. With pseudo real-time wave input

The PRTWs with the wave speed of 6.0 m/s and the total length of 1060.2 m are simulated as shown in Fig. 9 (a). The corresponding wave height at a fixed point in the time domain is shown as Fig. 9 (b). The fluctuating tide with the average speed of 1.0 r/s is depicted in Fig. 9 (c). The simulation results of input force from waves, input torque from tidal currents and output voltage are presented in Fig. 10. When the wave input velocity reaches 2.34 m/s and the total resistance is 1.0 kΩ, the input force is 1.25 kN and input torque is 4.74 N m. The output voltage is 394.9 V. The overall efficiency of 20.3 % is achieved from the average input power of 402.8 W and average output power of 81.5 W. The ratio of min-max voltage without overrunning phase and with overrunning phase is 0.30 and 0.58 respectively. The overrunning phase results in a 27.3 % improvement in average output voltage and a 54.0 % improvement in average output power in this case. After eliminating the influence of tidal energy (i.e., setting the tidal module input to 0), the average output voltage and average output power of the wave module increase by 67.0 % and 121.1 % respectively, due to the overrunning phase. The overrunning phase can be observed in the partial enlargement in Fig. 10 (c). In acceleration, the curves coincide, which is called meshing phase. While in deceleration, the output velocity with overrunning phase decreases more slowly than without it, resulting in smoother output voltage and higher output power. When the following speed peak is much smaller than the previous one, the curve with overrunning phase even skips the small peak ("skip peak") but with a decrease in slope, since the damping decreases during the small peak.

Wave speeds of 3.53 m/s, 5.30 m/s and 10.60 m/s (i.e., the average wave periods of 6.0 s, 4.0 s and 2.0 s) are also simulated to compare the contribution of overrunning phase under different conditions (Fig. 11). As wave speeds increase, the overrunning phase improves the output power by 28.48 %, 47.16 % and 91.77 % respectively. Meanwhile, the overrunning phase occurs more often or for a longer duration under conditions with larger wave speeds (Fig. 11 (a)), resulting in more "skip peak" (Fig. 11 (b)).

In summary, the simulation results with sine wave and pseudo real-time wave input validate both the discretization modeling methodology and the feasibility of the HWTEC proposed in this work. By comparing the energy conversion under sine wave input and PRTW input, it is observed that the output power and efficiency are lower with PRTW input than with sine wave input. It aligns with the conclusions from the real ocean experiments in previous work [26]. The lower performance with PRTW input can be attributed to the greater randomness and instability of real ocean waves compared to sine waves. Since output power is proportional to the square of output speed, fluctuations of input speed are amplified in the output power, resulting in reduced efficiency. Nonetheless, the improvement in stability and efficiency introduced by the overrunning mechanism remains significant. Hence, the discretization modeling method, which is compatible with random wave input and real ocean wave data, is crucial for minimizing the distortions caused by using idealized sine wave inputs.

6. Conclusion

The discretization modeling methodology is proposed in this work for more efficient dynamic analysis of Hybrid Wave-tidal Energy Converters (HWTEC). Combined with the Pseudo Real-Time Wave (PRTW) simulation method based on random wave theory, it can solve the nonlinear dynamic characteristics of the energy converter in the time domain under random wave conditions, getting rid of the dependence on continuous input and ideal sinusoidal waves. The hybrid wave-tidal energy converter proposed in this paper can utilize the complementarity between wave and tidal energies and the inherent nonlinear characteristics of the device to improve the output power and output stability.

(1) Compared to previous modeling methods, the discretization modeling can automatically complete the judgment and calculation of the nonlinear dynamic response in overrunning phase, closely reflecting the actual characteristics of ocean waves. It allows the direct numerical solution of nonlinear input and output parameter curves in the time domain, eliminating the complex and unreliable manual judgment and result back-substitution. Additionally, by using pseudo real-time wave

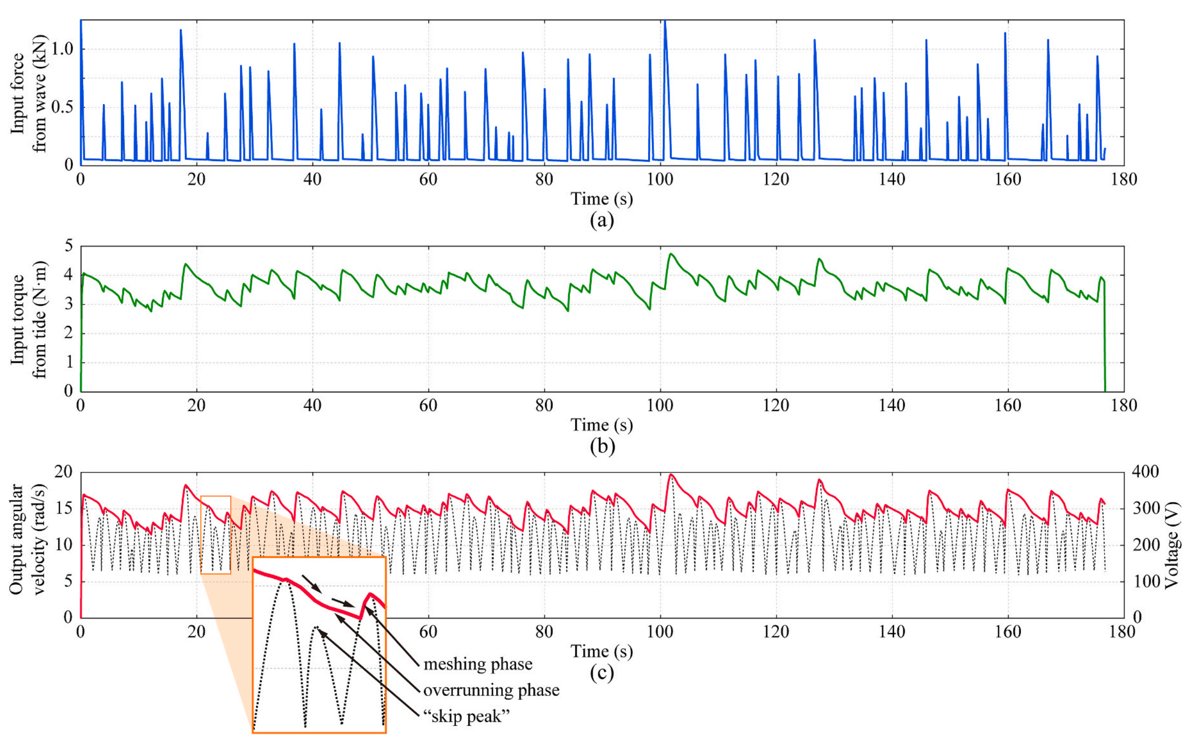

Fig. 10. (a) Input force from wave. (b) input torque from tide. (c) Output velocity and voltage.

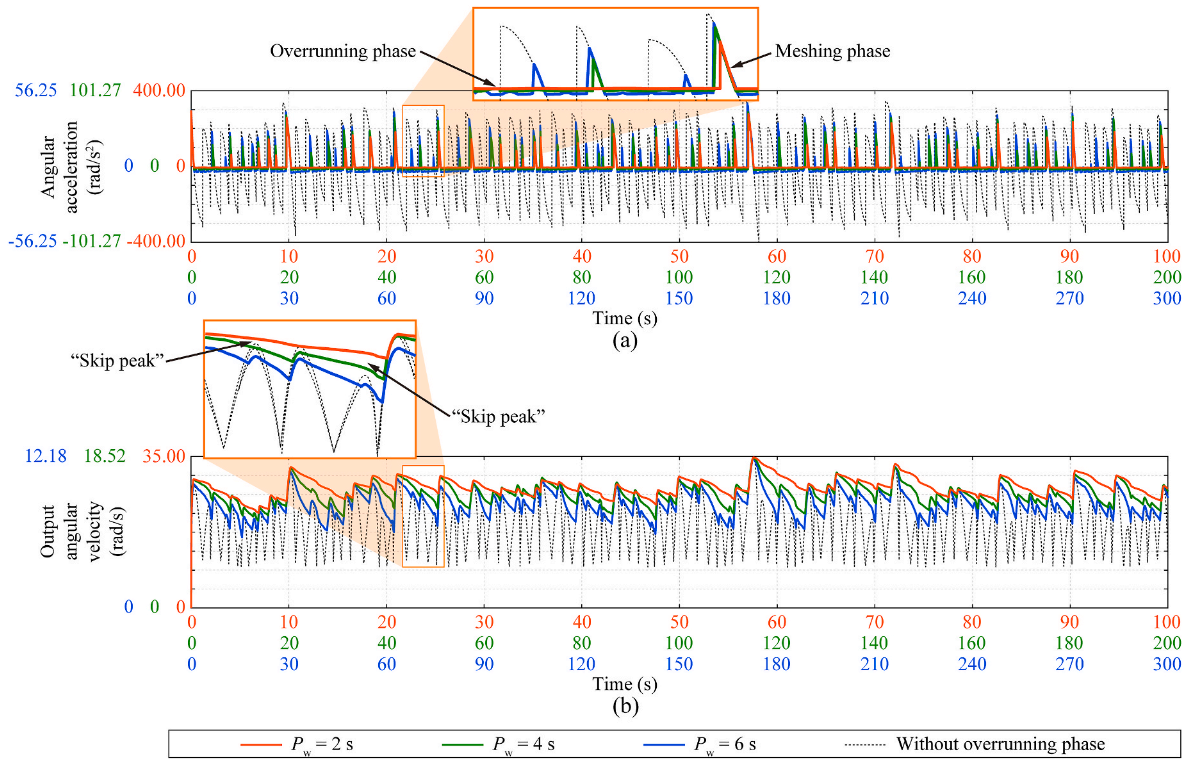

Fig. 11. Different wave period. (a) Angular acceleration. (b) Output angular velocity.

input, it also alleviates the distortion of ideal wave input and the limitation of continuous input function.

(2) The discretization modeling methodology is validated by simulating previous work again. There is the error of approximately 5 % in input and of 0.5 % in output occurs compared to previous methods. Considering previous experiment results, the outcomes of discretization modeling are actually closer to the performance observed in experiments.

(3) The hybrid wave-tidal energy converter, based on mechanical motion rectifier (MMR) and bevel gearbox, can rectify the reciprocating motion from waves into one-way linear motion and couple it with the one-way rotation from tides to generate higher power. Additionally, the coupling of tidal energy and wave energy takes advantage of the uneven and asynchronous distribution of them, enhancing output stability. This is particularly significant for applications requiring voltage stability, such as offshore platform microgrids and power supplies for offshore hydrogen electrolyzers.

(4) The simulation of the hybrid wave-tidal energy converter reveals the impact of key parameters on output power and efficiency. The average output power of 206.2 W and the efficiency of 40.4 % are obtained in sine wave input case. The average output power of 81.5 W and the efficiency of 20.3 % are obtained in pseudo real-time wave input case. The introduction of the overrunning phase increases output power by 54.0 % and significantly enhances output stability.

However, due to the lack of tidal current observation data, the fluctuating input tidal velocity in this work is simplified as a superposition of sine waves. While it is adequate for validating the modeling method and device design, more realistic tidal current velocity data is necessary for accurate simulations. Additionally, it is found that different random numbers inputs lead to variations in final power and efficiency, despite using the same wave height and wave speed. It is understandable over the time span of several minutes, but the potential errors and distortions it may cause are still unknown. In future work, further research over a longer time span can be conducted with investigating the relationship between energy density and power to address above problem and help generalize the modeling method. Furthermore, a prototype of the hybrid wave-tidal energy converter is currently being developed for experimental validation. The unique challenges arise from its vertically extensive design for capturing both tidal and wave energy. Further advancements in waterproofing and corrosion resistance are essential for its practical implementation. Regarding deployment locations, the hybrid wave-tidal energy converter is likely best suited for areas where both wave and tidal energy resources are abundant and exhibit comparable power magnitudes.

CRediT authorship contribution statement

Peihao Chen: Writing – review & editing, Writing – original draft, Validation, Methodology, Investigation, Formal analysis, Data curation, Conceptualization. **Dawei Wu:** Writing – review & editing, Supervision, Resources, Project administration, Funding acquisition, Formal analysis. **Yiqing Yang:** Writing – review & editing, Supervision, Resources, Data curation. **Athanasios Tsolakis:** Supervision, Resources, Project administration, Funding acquisition.

Declaration of competing interest

The authors declare that they have no known competing financial interests or personal relationships that could have appeared to influence the work reported in this paper.

Acknowledgements

The authors are thankful for the financial support from the EPSRC (the Engineering and Physical Sciences Research Council) of the United Kingdom via the research project EP/X038823/2.

Appendix A. Detailed simulation results

The amplitude A and frequency f of waves, along with the input tidal velocity R_2, determine the input power and output voltage directly. Fig. A1 - A3 present the detailed simulation results with different values to explore their respective influences.

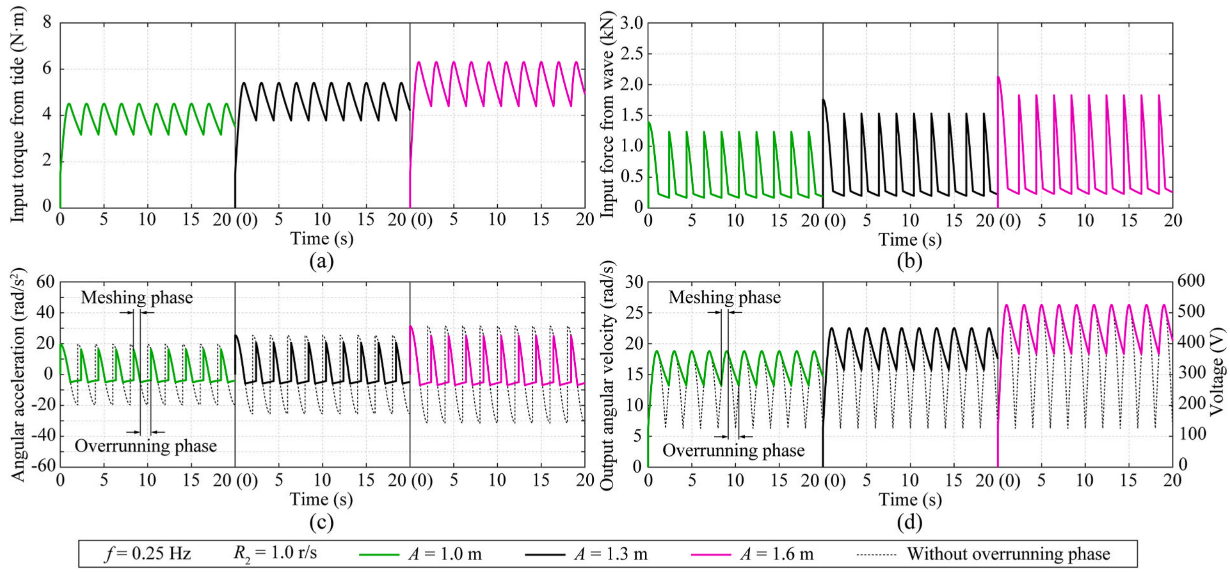

Fig. A1. Simulation results with different wave amplitude A.

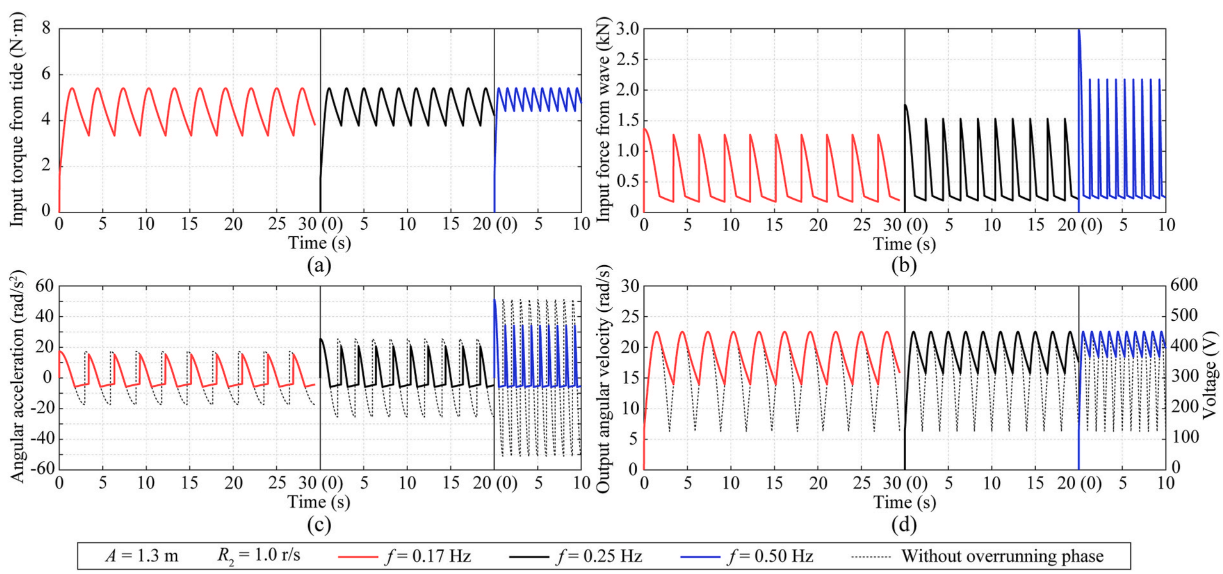

Fig. A2. Simulation results with different wave frequency f.

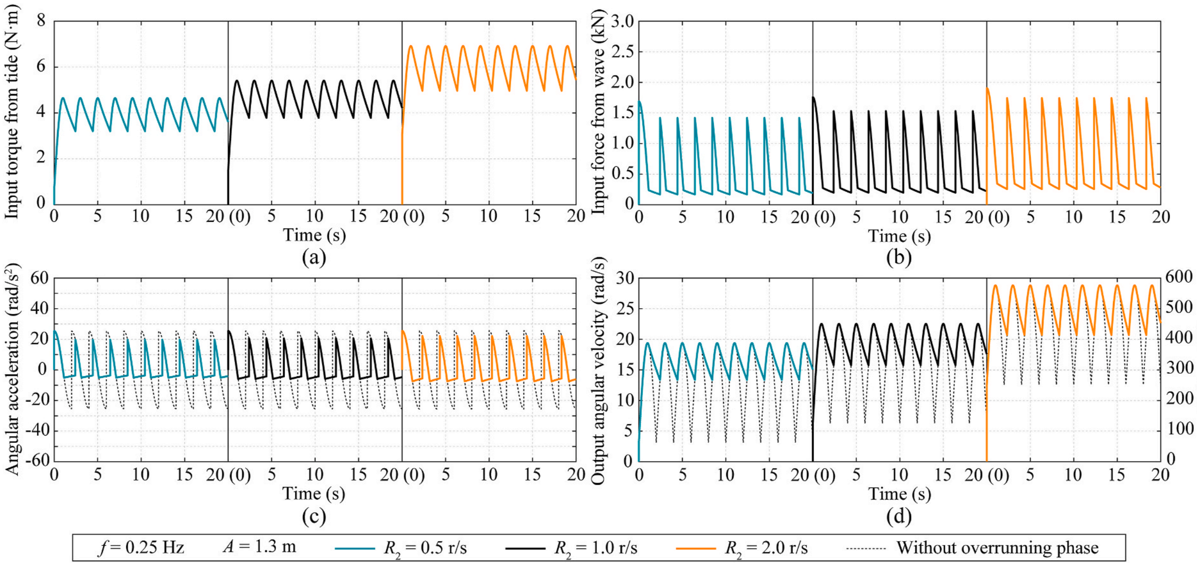

Fig. A3. Simulation results with different tide input velocity R_2.

Data availability

Data will be made available on request.

References

[1] Khan N, Kalair A, Abas N, Haider A. Review of ocean tidal, wave and thermal energy technologies. Renew Sustain Energy Rev 2017;72:590–604. https://doi.org/10.1016/j.rser.2017.01.079.

[2] Al Shami E, Zhang R, Wang X. Point absorber wave energy harvesters: a review of recent developments. Energies 2019;12(1):47. https://doi.org/10.3390/en12010047.

[3] Hu H, Xue W, Jiang P, Li Y. Bibliometric analysis for ocean renewable energy: an comprehensive review for hotspots, frontiers, and emerging trends. Renew Sustain Energy Rev 2022;167:112739. https://doi.org/10.1016/j.rser.2022.112739.

[4] Li X, Martin D, Liang C, Chen CA, Parker RG, Zuo L. Characterization and verification of a two-body wave energy converter with a novel power take-off. Renew Energy 2021;163:910–20. https://doi.org/10.1016/j.renene.2020.08.113.

[5] Li X, Liang C, Chen CA, Xiong Q, Parker RG, Zuo L. Optimum power analysis of a self-reactive wave energy point absorber with mechanically-driven power take-offs. Energy 2020;195:116927. https://doi.org/10.1016/j.energy.2020.116927.

[6] Liang C, Ai J, Zuo L. Design, fabrication, simulation and testing of an ocean wave energy converter with mechanical motion rectifier. Ocean Eng 2017;136:190–200. https://doi.org/10.1016/j.oceaneng.2017.03.024.

[7] Li H, Wu J, Shi X, Kong L, Kong W, Zhang Z, et al. A self-powered smart wave energy converter for sustainable sea. Mech Syst Signal Process 2024;220:111641. https://doi.org/10.1016/j.ymssp.2024.111641.

[8] Clemente D, Rosa-Santos P, Taveira-Pinto F. On the potential synergies and applications of wave energy converters: a review. Renew Sustain Energy Rev 2021;135:110162. https://doi.org/10.1016/j.rser.2020.110162.

[9] Silva RN, Nunes MM, Oliveira FL, Oliveira TF, Brasil ACP, Pinto MSS. Dynamical analysis of a novel hybrid oceanic tidal-wave energy converter system. Energy 2023;263:125933. https://doi.org/10.1016/j.energy.2022.125933.

[10] Chen P, Wu D. A review of hybrid wave-tidal energy conversion technology. Ocean Eng 2024;303:117684. https://doi.org/10.1016/j.oceaneng.2024.117684.

[11] Yin X, Zhao X, Zhang W. A novel hydro-kite like energy converter for harnessing both ocean wave and current energy. Energy 2018;158:1204–12. https://doi.org/10.1016/j.energy.2018.03.121.

[12] Calheiros-Cabral T, Clemente D, Rosa-Santos P, Taveira-Pinto F, Ramos V, Morais T, et al. Evaluation of the annual electricity production of a hybrid breakwater-integrated wave energy converter. Energy 2020;213:118845. https://doi.org/10.1016/j.energy.2020.118845.

[13] Chen S, Jiang B, Li X, Xiong Q, Huang J, Zuo L. Design and dynamics of hybrid wave and current energy converter. In: Proceedings of the ASME 2019 international design engineering technical conferences and computers and information in engineering conference, anaheim, California, USA, august 18–21. ASME; 2019. https://doi.org/10.1115/DETC2019-98040. V008T10A018.

[14] Jiang B, Li X, Chen S, Xiong Q, Chen B, Parker RG, et al. Dynamics of a hybrid wave-current energy converter with a novel power take-off mechanism. In: Proc. SPIE 10967, active and passive smart structures and integrated systems XIII, 109670U; 2019. https://doi.org/10.1117/12.2514186. Denver, Colorado, USA, March 21.

[15] Jiang B, Li X, Chen S, Xiong Q, Chen B, Parker RG, et al. Performance analysis and tank test validation of a hybrid ocean wave-current energy converter with a single power takeoff. Energy Convers Manag 2020;224:113268. https://doi.org/10.1016/j.enconman.2020.113268.

[16] Park M-S, Lee S-H, Ko S-C. Experimental capture width ratio on unit module system of hybrid wave energy converter for nearshore. Appl Sci 2022;12(12):5845. https://doi.org/10.3390/app12125845.

[17] Cheng Y, Dai S, Dai S, Ji C, Collu M, Yuan Z, et al. Energy conversion and hydrodynamic analysis of multi-degree-of-freedom wave energy converters integrated into a semi-submersible platform. Energy Convers Manag 2022;252:115075. https://doi.org/10.1016/j.enconman.2021.115075.

[18] Cheng Y, Fu L, Dai S, Collu M, Cui L, Yuan Z, et al. Experimental and numerical analysis of a hybrid WEC-breakwater system combining an oscillating water column and an oscillating buoy. Renew Sustain Energy Rev 2022;169:112909. https://doi.org/10.1016/j.rser.2022.112909.

[19] Cheng Y, Gong J, Zhang J. Hydrodynamic investigation on a single-point moored offshore cage-wave energy converter hybrid system. Ocean Eng 2024;299:116848. https://doi.org/10.1016/j.oceaneng.2024.116848.

[20] Pan Q, Wang B, Zhang L, Li Z, Yang Z. Whisk-inspired motion converter for ocean wave energy harvesting. IEEE ASME Trans Mechatron 2022;27(3):1808–11. https://doi.org/10.1109/TMECH.2021.3093939.

[21] Xie Q, Zhang T, Pan Y, Zhang Z, Yuan Y, Liu Y. A novel oscillating buoy wave energy harvester based on a spatial double X-shaped mechanism for self-powered sensors in sea-crossing bridges. Energy Convers Manag 2020;204:112286. https://doi.org/10.1016/j.enconman.2019.112286.

[22] Dai Y, Chen Y, Xie L. A study on a novel two-body floating wave energy converter. Ocean Eng 2017;130:407–16. https://doi.org/10.1016/j.oceaneng.2016.11.049.

[23] Li X, Chen C-A, Chen S, Xiong Q, Huang J, Lambert S, et al. Dynamic characterization and performance evaluation of a 10-kW power take-off with mechanical motion rectifier for wave energy conversion. Ocean Eng 2022;250:110983. https://doi.org/10.1016/j.oceaneng.2022.110983.

[24] Martin D, Li X, Chen C-A, Thiagarajan K, Ngo K, Parker R, et al. Numerical analysis and wave tank validation on the optimal design of a two-body wave energy converter. Renew Energy 2020;145:632–41. https://doi.org/10.1016/j.renene.2019.05.109.

[25] Yang Y, Pian Y, Liu Q. Design of energy harvester using rotating motion rectifier and its application on bicycle. Energy 2019;179:222–31. https://doi.org/10.1016/j.energy.2019.05.036.

[26] Yang Y, Chen P, Liu Q. A wave energy harvester based on coaxial mechanical motion rectifier and variable inertia flywheel. Appl Energy 2021;302:117528. https://doi.org/10.1016/j.apenergy.2021.117528.

[27] Chen P, Yang Y. Design, dynamics modeling, and experiments of a vibration energy harvester on bicycle. IEEE ASME Trans Mechatron 2023;28(5):2670–8. https://doi.org/10.1109/TMECH.2023.3246516.

[28] Wang C-C, Yen C-E, Chen C-L, Wu J-X, Liu P. Ocean wave simulation in real-time using GPU. In: 2010 international computer symposium (ICS2010); 2010. p. 419–23. https://doi.org/10.1109/COMPSYM.2010.5685474. Tainan, Taiwan, December 16-18.

[29] Weerasinghe M, Sandaruwan D, Keppitiyagama C, Kodikara N. A novel approach to simulate wind-driven ocean waves in the deep ocean. In: International conference on advances in ICT for emerging regions (ICTer); December 11-15,

2013. p. 28–37. https://doi.org/10.1109/ICTer.2013.6761151. Colombo, Sri Lanka.
[30] Lu J, Wang D. An Ocean wave simulation research based on controllable FBM model. In: 2010 6th international conference on wireless communications networking and mobile computing (WiCOM); September 23-25, 2010. p. 1–3. https://doi.org/10.1109/WICOM.2010.5601318. Chengdu, China.
[31] Li Z, Wang H. Ocean wave simulation based on wind field. PLoS One 2016;11(1): e0147123. https://doi.org/10.1371/journal.pone.0147123.
[32] Liang Y-J, Guo F-L, Chen X-L. High-precision and large scale dynamic of real-time ocean waves simulation. In: Proceedings of 2013 3rd international conference on computer science and Network technology; 2013. p. 165–9. https://doi.org/10.1109/ICCSNT.2013.6967087. Dalian, China, October 12-13, 2013.
[33] Guo Q, Xu Z. Simulation of deep-water waves based on JONSWAP spectrum and realization by MATLAB. In: 2011 19th international conference on Geoinformatics1; June 24-26, 2011. p. 1–4. https://doi.org/10.1109/GeoInformatics.2011.5981100. Shanghai, China.
[34] Roy A, Auger F, Dupriez-Robin F, Bourguet S, Tran QT. Electrical power supply of remote maritime areas: a review of hybrid systems based on marine renewable energies. Energies 2018;11(7):1904. https://doi.org/10.3390/en11071904.
[35] World Meteorological Organization. Guide to wave analysis and forecasting. second ed. Geneva, Switzerland: Secretariat of the World Meteorological Organization; 1998. https://doi.org/10.25607/OBP-1523. 159pp (WMO-No. 702).
[36] Yildirim B, Karniadakis GE. Stochastic simulations of ocean waves: an uncertainty quantification study. Ocean Model 2015;86:15–35. https://doi.org/10.1016/j.ocemod.2014.12.001.